# Combined electrochemical impedance spectroscopy and X-ray photoelectron spectroscopy analysis of the passive films formed on 5083 aluminium alloy

C. Nkoua, Jérôme Esvan, Bernard Tribollet, Régine Basséguy, Christine Blanc

## To cite this version:

C. Nkoua, Jérôme Esvan, Bernard Tribollet, Régine Basséguy, Christine Blanc. Combined electrochemical impedance spectroscopy and X-ray photoelectron spectroscopy analysis of the passive films formed on 5083 aluminium alloy. Corrosion Science, 2023, 221, pp.111337. 10.1016/J.CORSCI.2023.111337 . hal-04158262

HAL Id: hal-04158262
https://hal.science/hal-04158262v1

# Combined electrochemical impedance spectroscopy and X-ray photoelectron spectroscopy analysis of the passive films formed on 5083 aluminium alloy

**C. Nkoua[1], J. Esvan[1], B. Tribollet[2], R. Basseguy[3], C. Blanc[1,*]**

[1]CIRIMAT, Université de Toulouse, CNRS, INP-ENSIACET, 4 allée Emile Monso, CS 44362, 31030 Toulouse cedex 4, France

[2]LISE UMR 8235, CNRS-Sorbonne Universités, 4 place Jussieu BP 133, 75252 Paris, France

[3]LGC, Université de Toulouse, CNRS, INP, UPS, 4 allée Emile Monso, CS 44362, 31030 Toulouse cedex 4, France

*Corresponding author. Tel./fax: +33 (0)5 34 32 34 07 / +33 (0)5 34 32 34 98
E-mail address: christine.blanc@toulouse-inp.fr

**Abstract –** A combined electrochemical impedance spectroscopy (EIS) and X-ray photoelectron spectroscopy (XPS) approach showed that the corrosion behaviour of 5083 Al alloy was controlled by Mg dissolution at the Mg-rich intermetallic coarse particles (IMCs) that were defects of the passive film. It was thus shown that microstructures with high amount of Mg-rich IMCs were less resistant to corrosion. EIS experimental data were well superimposed with fitted ones calculated using a model proposed in the literature for pure magnesium. The model allowed to plot the resistivity profiles of the passive films, which highlighted their double-layer structure evidenced by XPS.

**Keywords –** A. aluminium; A. intermetallics; A. magnesium; B. EIS; B. XPS; C. passive films.

## 1. Introduction

The corrosion behaviour of Al-Mg alloys, e.g. 5083 alloy, has been largely studied in the literature because of their interest in terms of application in marine environment in particular [1-3]. Pitting corrosion is one of the most common forms of corrosion for these materials [2,4,5] although, depending on the precipitation at the grain boundaries, intergranular corrosion may be observed [6-11]. Most papers clearly show the detrimental role of intermetallics, in particular Mg-rich particles, on the corrosion behaviour of these alloys [12-14]. These particles have such a negative influence that the corrosion behaviour of the material is strongly improved when their density in the alloy is reduced [15]. We compared in a previous work the corrosion behaviour of two plates of 5083 Al-Mg alloy, and we showed that the plate with the lower fraction of surface area covered by Mg-rich particles evidenced a better corrosion behaviour [16]. Insofar as reference is made to pitting corrosion, it is clear that this can be interpreted by considering that these particles constitute defects in the passive film [17-18]. X-ray photoelectron spectroscopy (XPS) analyses of the native oxide films and /or passive films formed on Al-Mg alloys showed the incorporation of Mg species into these films, demonstrating the electrochemical activity of the Mg-rich particles [19], with relevant comparison with the oxide films formed on magnesium and Mg-containing intermetallics [20,21]. Similarly, Yao *et al.* showed, for Zn-Mg-Al alloys, that the incorporation of Mg led to significant changes in the nature of the corrosion products and variations in the electrochemical impedance spectroscopy (EIS) response [22].

Literature demonstrated the interest of EIS for the analysis of the electrical properties of the passive films for Al-Mg alloys [23], and more globally for metallic materials [24,25]. However, as for all techniques and methods, the interest of EIS relies on a relevant use of the experimental data, which requires to analyse them using models providing a meaningful description of the electrochemical system. In particular, it is important to consider the gradients in electrical properties of the passive films from the metal/passive film interface to the passive film/electrolyte interface. For Al-Mg alloys in particular, considering the reactivity of the Mg-rich particles and the incorporation of Mg species into the passive films, this is of major importance to give a relevant description of the corrosion behaviour of these alloys. Different models exist that can describe a passive film layer considered as a dielectric layer, and that takes into account the gradient in electrical resistivity of the passive film. Among those models, the Young and power-law models were clearly described by Tribollet *et al.* [25].

The objective of the present manuscript is to complete the first approach of the corrosion behaviour of the two plates of 5083 Al-Mg alloy presented in a previous work [16], and based essentially on the analysis of polarisation curves. The corrosion behaviour of the 5083 Al-Mg alloy was analysed here by focusing on the properties of the passive films by combining EIS measurements and XPS analyses of these films, taking care to establish a clear relationship with the electrochemical behaviour of the Mg-rich particles. The resistivity profiles of the passive films were compared with the profiles in chemical composition obtained by XPS.

## 2. Experimental

### 2.1. *Materials*

Experiments were performed using the 1 mm and 7 mm plates of Al-Mg 5083 H111 alloy described in our previous work [16]. Their chemical composition is shown in Table 1. For brevity reasons, only the main results concerning the microstructures of the two plates are reminded hereafter. A recrystallised microstructure with equiaxed grains of 28 ± 2 µm and 31 ± 1 µm was observed in the rolling plane, *i.e.* L (longitudinal) – LT (long transverse) plane, for the 1 mm and 7 mm plates, respectively. A gradient in microstructure was observed in the ST (short transverse) direction for the 7 mm plate: observations of the LT-ST plane showed a recrystallised microstructure near the surface of the plate (grain size of 29 ± 6 µm), whereas grains elongated in the LT direction (average length of 35 ± 13 µm) were observed in the core of the plate. In the following, samples corresponding to the rolling plane of the plates will be referred to as 1 mm L-LT and 7 mm L-LT. The 7 mm LT-ST samples will correspond to specimens extracted from the 7 mm plate, with the LT-ST plane exposed to the electrolyte during electrochemical tests. For the two plates, coarse intermetallic particles (IMCs) were observed: Mg-rich IMCs, containing also Si, and Al-Fe-Mn IMCs. The fraction of surface area covered by the IMCs was higher for the 7 mm plate compared to the 1 mm plate, which was in agreement with the higher amounts of Mg, Si, Fe and Mn in the 7 mm plate.

**Table 1**: Chemical composition of the Al-Mg 5083 H111 alloy (wt. %)

| | Mg | Mn | Fe | Si | Cr | Cu | Zn | Ti | Al |
|---|---|---|---|---|---|---|---|---|---|
| **1 mm** | 4.35 | 0.50 | 0.22 | 0.11 | 0.067 | 0.065 | 0.018 | 0.016 | Balance |
| **7 mm** | 4.70 | 0.59 | 0.37 | 0.32 | 0.110 | 0.060 | 0.070 | 0.030 | Balance |

### 2.2. *EIS measurements*

EIS measurements were performed in a 0.001 M NaCl + 0.1 M $Na_2SO_4$ solution open to air and maintained at 25 ± 2 °C. A three-electrode cell was used with an Ag/AgCl/KCl (saturated) electrode as reference, and a platinum foil as counter electrode. In the manuscript, all potentials are quoted in relation to the saturated calomel electrode (SCE) for easy comparison with literature data. Specimens were 45-mm diameter discs for the L-LT plane, for both the 1 mm and 7 mm plates, while parallelepipeds (20 x 7 $mm^2$ rectangular surface in the LT-ST plane) were machined from the 7 mm plate to study the electrochemical behaviour of the LT-ST plane. The 1 mm L-LT and 7 mm LT-ST samples were mounted into an epoxy resin with a Cu wire for electrical connection. Before EIS measurements, all samples were ground with SiC paper down to 240. Then, they were vertically positioned in the electrochemical cell and immersed at their open circuit potential (OCP). Apart from some specific tests, all EIS measurements were performed at OCP. The frequency range was from $10^5$ Hz to $10^{-3}$ Hz with 6 points per decade, and the potential modulation amplitude was 20 mV. Each average impedance value was calculated with 3 measurements per point. EIS measurements were performed after 24, 72, 168 (7 days), and 336 h (14 days) of immersion at OCP in such a way that, for all measurements, the electrochemical system was considered in a stationary state. For all conditions, EIS measurements were repeated three times for reproducibility reasons.

The impedance data were regressed using a computer program allowing measurement model analysis [26] to remove the experimental data inconsistent with the Kramers-Kronig relations. Then, the resulting data were regressed by an in-house simplex regression program.

### 2.3. *XPS analyses*

The native oxide film and the passive films formed after 24 h and 144 h (6 days) on the 1 mm L-LT sample (sample of 10 x 5 $mm^2$) were analysed by XPS using a Thermo Kalpha apparatus, equipped with a monochromatised Al-Kα source (hν = 1486.6 eV). The X-ray spot surface area was about 400 μm in diameter. The pressure was 2.2 $10^{-7}$ mbar in the analysis chamber with flood gun to neutralise charge effects. First, for all samples, survey spectra were obtained with a 160 eV pass energy and 1 eV step. Then, high-resolution spectra were recorded with a 30 eV pass energy and 0.1 eV step for C 1s, O 1s, Al 2p, and Mg 2p. Depth profiles were also performed upon Ar+ etching (500 eV) for high-resolution C 1s, O 1s, Al 2p, and Mg 2p spectra, with a pass energy of 30 eV. All photoelectron spectra were analysed with built-in Avantage software (Thermo), and a Shirley background was systematically subtracted. The binding energy scale was calibrated using the carbon C1s at 284.6 eV (± 0.1 eV).

## 3. Results

### 3.1. Qualitative analysis of EIS measurements

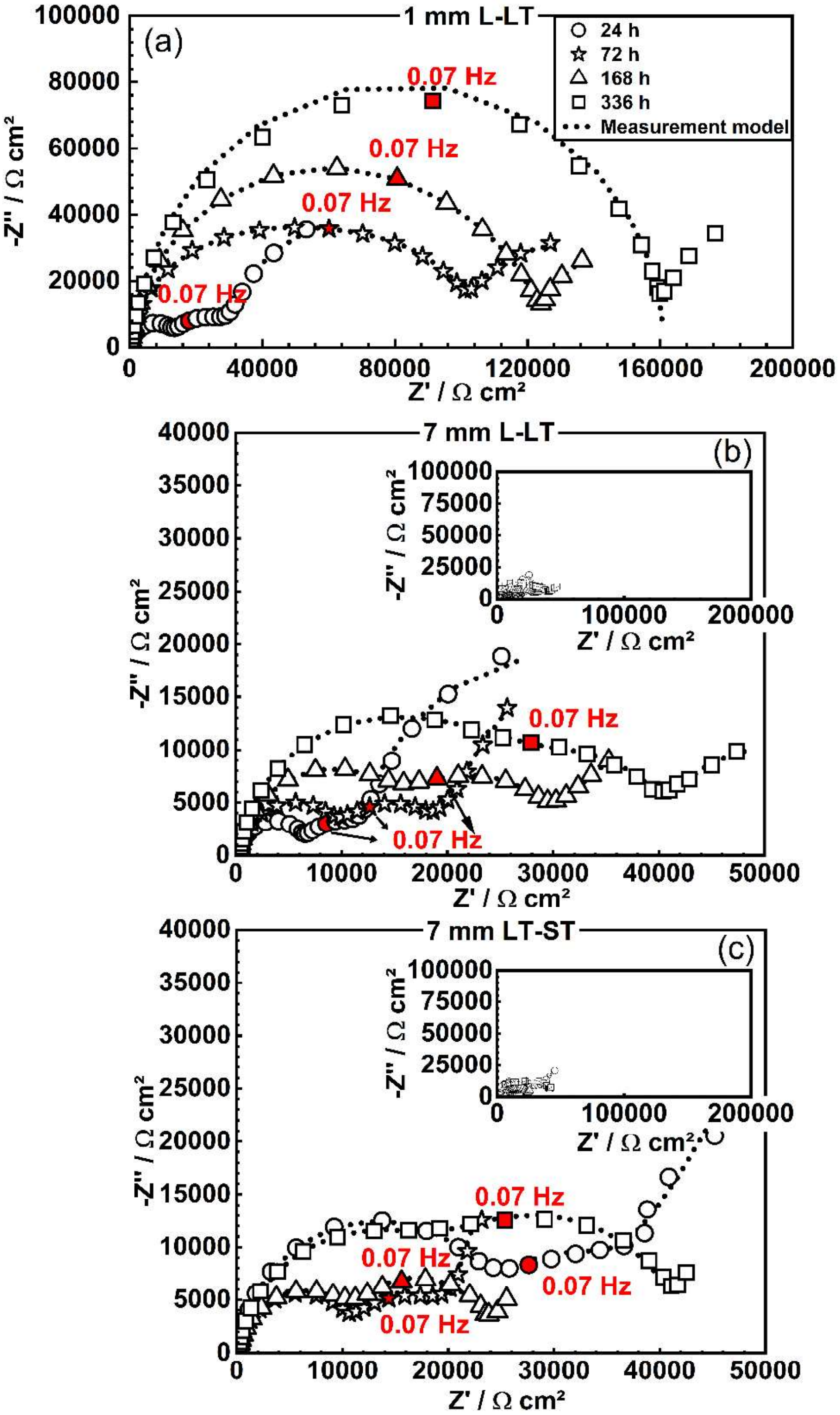

**Figure 1.** Impedance diagrams (Nyquist coordinates) plotted for a) 1 mm L-LT, b) 7 mm L-LT and c) 7 mm LT-ST samples in 0.1 M $Na_2SO_4$ + 0.001 M NaCl at $E_{corr}$, for different immersion times (24 h, 72 h, 168 h and 336 h). Inserts in Fig. 1 b) and c) show the impedance diagram plotted for 7 mm L-LT and 7 mm LT-ST samples, respectively, with the same scale as for 1 mm L-LT sample in Fig. 1 a), allowing a better comparison of the impedance data. The measurement model was regressed to the experimental data.

Fig. 1 shows the impedance diagrams plotted in Nyquist coordinates for the 1 mm L-LT, 7 mm L-LT and 7 mm LT-ST samples after different immersion times at $E_{corr}$ in the chloride containing sulphate solution. For the 7 mm L-LT and 7 mm LT-ST samples, independently of the immersion times, all the diagrams were characterised by three capacitive loops. For the 1 mm L-LT sample, three capacitive loops were observed after 24 h of immersion at $E_{corr}$, while only two capacitive loops could be distinguished in the frequency range analysed when the immersion time increased, due to a significant increase in the size of the loops at high and medium frequencies. Interestingly, the size of the capacitive loops, in particular this one at high frequency, was significantly greater for the 1 mm L-LT sample than for the 7 mm L-LT and LT-ST samples, whatever the immersion times, whereas the size of the capacitive loops was quite similar for both 7 mm samples. This preliminary observation suggested that the corrosion resistance of the 1 mm L-LT sample in the chloride containing solution was higher than for the 7 mm L-LT samples, in agreement with our previous results deduced from the analysis of potentiodynamic polarisation curves [16]. The improved corrosion resistance of the 1 mm L-LT sample had been attributed to a lower amount of Al-Fe-Mn and Mg-rich IMCs compared to the 7 mm samples, in agreement with literature data showing that these IMCs destabilised the passive film [12,13,17,18,27].

After this preliminary graphical analysis of the impedance data, we used the measurement model [28-31] and the corresponding software [26] to quantify the error structure of these data and eliminate the inconsistent ones. Then, we used the information obtained to regress the process model to the experimental data. The methodology applied is described below considering the 1 mm L-LT sample after 24 h of immersion at $E_{corr}$, as a representative example (Fig. 2a). The same methodology was used for all the samples and immersion times (Fig. 1).

The measurement model corresponds to a circuit model consisting of a solution resistance $R_e$ in series with a number of Voigt elements. The Voigt elements include a resistor in parallel with a capacitor. The regression of the Voigt measurement model allows the determination of polarisation resistance, ohmic resistance and capacitance values at infinite frequency from EIS data [32]. In the present study, because we were interested in the properties of the oxide films grown on the sample surface, we only gave attention to $R_e$ values and the capacitance value C when the frequency tends towards infinity. The C value obtained for the 1 mm L-LT sample, equal to 5.6 ± 0.2 µF cm$^{-2}$, was perfectly relevant with a few nm thick passive layer, considering a dielectric constant ε value of 11.5 characteristic of an alumina film, and the classical permittivity of vacuum $\varepsilon_0$ value (8.85 10$^{-14}$ F/cm) [25]. Then, the experimental data were plotted as complex capacitance (Fig. 2b) which allows the capacitance value at infinite frequency to be graphically determined. The value obtained, i.e. 5.1 µF cm$^{-2}$, was in good agreement with the C value deduced from the measurement model, confirming the good quality of the experimental data, as shown by the very good superimposition between both fitted and experimental data (Fig. 1 and Fig. 2a).

Fig. 2 c) and d) show the experimental impedance data plotted in Bode coordinates for the 1 mm L-LT sample after 24 h at $E_{corr}$. Results are also plotted in ohmic-resistance corrected Bode plots, Z-$R_e$, where $R_e$ is the electrolyte resistance estimated from the measurement model (Fig. 2a). A CPE behaviour was evidenced in the medium frequency range, *i.e.* 1 to 100 Hz, while the phase of the corrected Bode plot (Fig. 2d) clearly showed in high frequency a variation characteristic of the ohmic impedance [33].

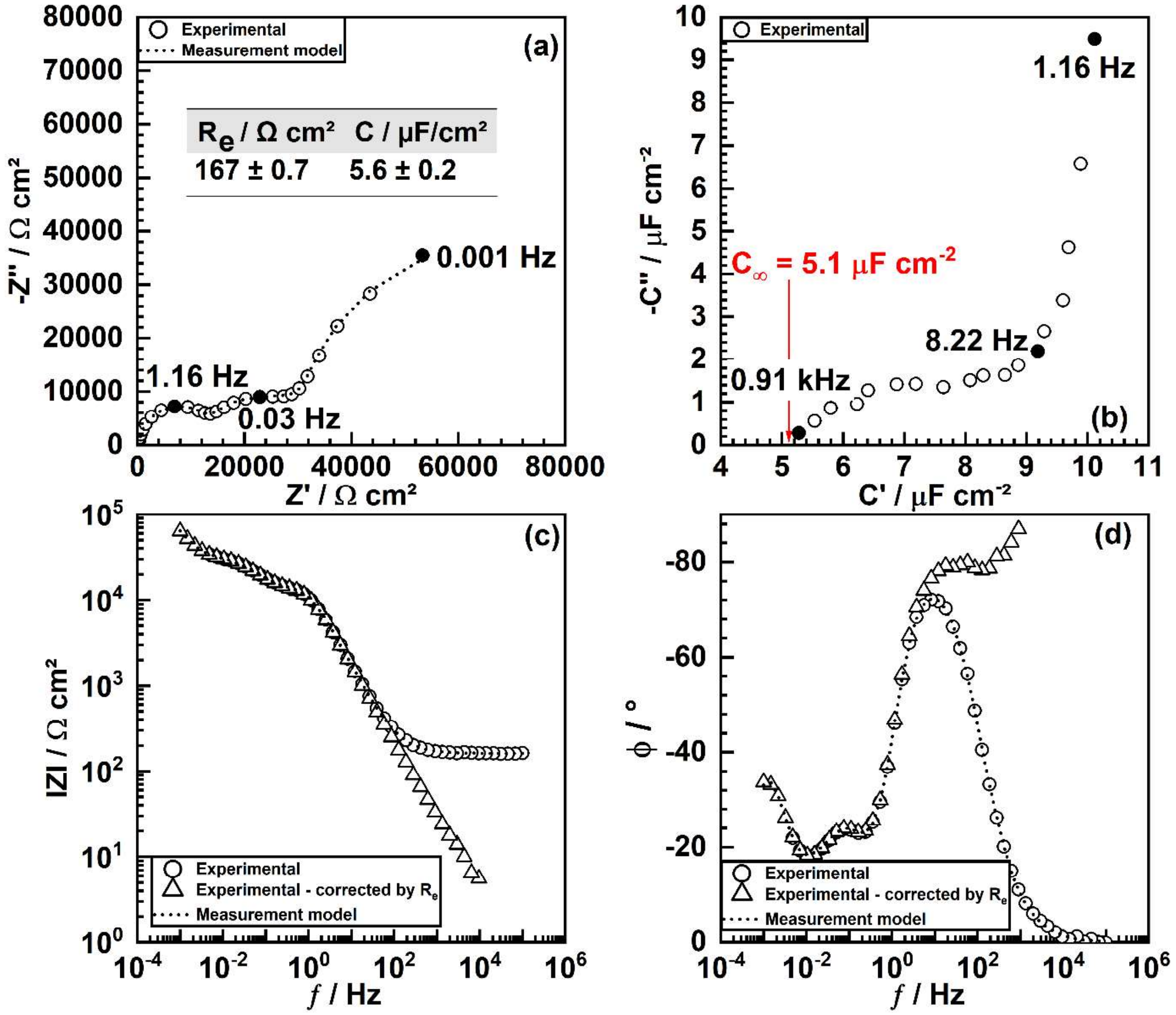

**Figure 2.** Impedance results obtained for the 1 mm L-LT sample after 24 h of immersion in 0.1 M Na$_2$SO$_4$ + 0.001 M NaCl at $E_{corr}$. a) Impedance diagram in Nyquist coordinates. The table shows the electrolyte resistance and capacitance at infinite frequency calculated from the measurement model. b) Diagram in complex capacitance (experimental data). Impedance diagram in Bode coordinates with c) modulus and d) phase. The ohmic-resistance corrected Bode plots are added for comparison. The measurement model was regressed to the experimental data in Fig. 2 a), c) and d).

Finally, impedance diagrams were plotted at different potential values, i.e. $E_{corr}$, $E_{corr}$ – 100 mV, $E_{corr}$ + 100 mV and $E_{corr}$ + 200 mV for the 1 mm L-LT sample after 336 h (14 days) of immersion at $E_{corr}$ (Fig. 3). This corresponded to a first attempt to identify the elementary processes characteristic of the three capacitive loops. Results clearly showed a non-monotonous variation of the size of the capacitive loop at high frequency as a function of the potential applied, whereas the quality of the experimental data was assessed by the use of the measurement model. This led us to assume that this capacitive loop was not characteristic of a pure dielectric behaviour. Considering our previous results [16], and more globally literature data that showed dissolution processes occurring at Mg-rich IMCs in 5xxx series Al alloys [12,13,14,18,34,35], it was assumed that the passive film formed on the sample surface was disrupted at the Mg-rich IMCs [15,18]. This was associated with anodic dissolution processes at those IMCs leading to the formation of corrosion products above the Mg-rich IMCs [13,21,36]. This could contribute to explain the increase in the size of the capacitive loops when the immersion time increased due to the limitation of the anodic dissolution processes with the accumulation of the corrosion products (Fig. 1). The same explanation was relevant to explain the non-monotonous variation of the size of the capacitive loop at high frequency with an increase in the potential applied when considering that this loop was characteristic of anodic faradic process. Indeed, the size of the capacitive loop was dependent on the potential effect: for an anodic dissolution process, it was expected to decrease when the potential was increased. However, it was also dependent on the active surface, some zones being blocked by the corrosion products [22].

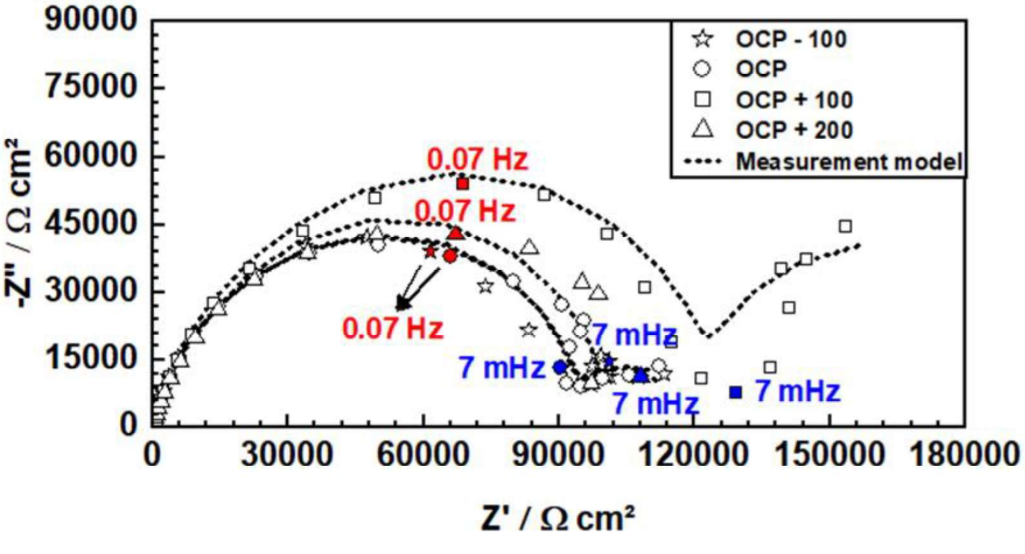

**Figure 3**. Impedance diagrams (Nyquist coordinates) plotted for the 1 mm L-LT sample after 336 h (14 days) of immersion in 0.1 M $Na_2SO_4$ + 0.001 M NaCl at $E_{corr}$. The diagrams were plotted at $E_{corr}$, $E_{corr}$ – 100 mV, $E_{corr}$ + 100 mV and $E_{corr}$ + 200 mV. The measurement model was regressed to the experimental data.

This suggested that further modelling of the impedance data should consider the electrochemical and chemical processes occurring at the Mg-rich IMCs. Therefore, the passive films formed on the 1 mm L-LT sample after both short and long immersion times in the chloride-containing solutions were analysed by using XPS in order to allow a physically meaningful model to be developed for the analysis of the impedance data. XPS analyses were also performed on a polished sample in order to analyse the native oxide film for comparison with the passive films formed during immersion in the electrolyte.

### 3.2. XPS analysis of the passive films formed on 5083 Al alloy in chloride-containing sulphate solution

XPS analyses were performed on the 1 mm L-LT sample after polishing and after immersion at $E_{corr}$ in the chloride-containing solution for 24 h and 144 h (6 days). It was assumed that the results obtained with the 1 mm sample were representative of the behaviour of the 7 mm samples.

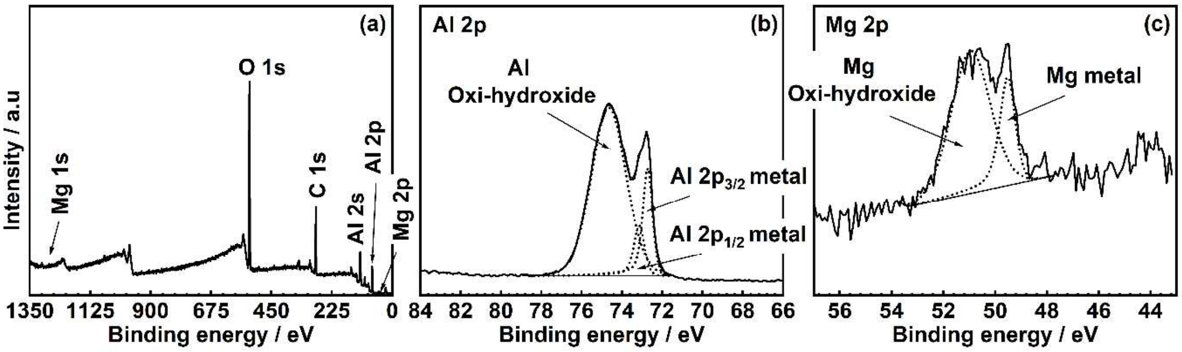

**Figure 4.** XPS analyses of the as-polished 1 mm L-LT sample a) Survey spectrum. High resolution b) Al 2p and c) Mg 2p core level spectra.

Fig. 4 a) shows the survey spectrum obtained for the as-polished sample, allowing the main elements present on the surface covered by the native oxide film to be identified, *i.e.* Al, Mg and O. The high resolution Al 2p and Mg 2p core level spectra are reported in Fig. 4 b) and c), respectively. The lower binding energy peaks at 72.7 and 73.1 eV in the Al 2p region were assigned to the metallic Al, *i.e.* Al $2p_{3/2}$ and Al $2p_{1/2}$ respectively, and the higher binding energy peak at 74.7 eV to the oxidised Al(III), in agreement with literature [21,37,38]. Observation of both metallic and oxidised components confirmed the presence of an oxide layer corresponding to the native oxide film. However, the detection of the metallic Al component showed that either the native oxide film was thinner than 10 nm, or that there were local areas where the oxide/hydroxide layer was thinner than 10 nm. Furthermore, in the Mg 2p region, one metallic Mg signal at a binding energy of 49.5 eV, and that of oxidised Mg at a binding energy of 51.0 eV [21,39-41] were observed, showing that the native oxide film formed on 5083 Al alloy incorporated Mg species, in agreement with literature data [19,42-46].

Fig. 5 shows the results obtained from a semi-quantitative analysis of the XPS data with concentration profiles (in at. %) plotted for Al(III) and metallic Al (Fig. 5 a)), Mg(II) and metallic Mg (Fig. 5 b)) as a function of the sputtering time. The Mg 2p, Al 2p and O 1s spectra of selected sputtering times are given as supplementary files (A1) to display the changes of the surface chemical states. The variation of the total amounts of Al and Mg and that of the ratio O/Al(III) are also plotted in Fig. 5 c), d) and e), respectively. For all the profiles, it is important to be careful with the data at 0 s of sputtering since surface pollutants can induce an error on the calculations of the concentrations. Both Al(III) (Fig. 5 a)) and Mg(II) (Fig. 5 b)) concentrations showed significant variations during the first 470 s of sputtering: they remained high during the first 250 s of sputtering, and then decreased significantly to reach a value of 3.8 at. % and 0.4 at. %, respectively, after 470 s of sputtering. Finally, they decreased much more slowly, and, after 2470 s of sputtering, the concentrations of Al(III) and Mg(II) were about 0.8 at. % and 0.3 at. %, respectively, showing that the contribution of the oxide/hydroxide film was almost negligible. Furthermore, Fig. 5 e) shows that the ratio O/Al also varied significantly during the first 470 s: it was about 1.8 in the first 250 s of sputtering, then dropped down to 1.5

after 470 s of sputtering. Finally, it remained almost stable at this value for longer sputtering times. The results led us to identify two main regions as a function of the intensity changes of the Al(III) and Mg(II) signals, as well as the evolution of the ratio O/Al(III): an oxide/hydroxide region followed by an intermediate region [47]. The first region that extended to 470 s of sputtering was assigned to the outer layer of the native oxide film, where Al could be found under an hydroxylated form, which could be AlO(OH), or a mixture of hydroxilated forms, without neglecting the contribution of an oxide form, i.e. $Al_2O_3$. In this region, a gradient in chemical composition was evidenced in the direction normal to the surface. Non-negligible amount of Mg(II) was detected in this outer layer, with a concentration of about 1.2 at. % of Mg(II) measured during the first 250 s of sputtering, confirming the incorporation of Mg species in the native oxide film. The intermediate region, ranging between 470 and 2470 s of sputtering, mixed the inner layer of the native oxide film and the metallic substrate. The chemical composition of the inner layer seemed more homogeneous compared to that of the outer layer: the ratio O/Al remained equal to 1.5 in such a way that the inner layer of the native oxide film seemed mostly composed of the oxide form of Al, i.e. $Al_2O_3$, while the contribution of Mg species was reduced at an almost stable value around 0.3 at. % [19]. It was important to note here that the accurate identification of the two regions was difficult due to the roughness of the sample, and the frontiers between each region, as plotted in Fig. 5, are given as an indication only. The stabilisation of the total amounts of Al and Mg at high intensity from 470 s confirmed that the intermediate region corresponded to both the inner layer and the bulk sample, even though a decreasing contribution of the inner layer of the oxide film with the increase in sputtering time could not be neglected. Finally, it was of interest to note that the incorporation of Mg species into the native oxide film was associated with a Mg depletion in the underlying metal since the metallic Mg concentration was only 2.5 at. % after 2470 s of sputtering to be compared to 4.8 at. % in the bulk metal. Nevertheless, additional analyses performed after 6000 s of sputtering (not shown) did not allow to measure the chemical composition expected for the bulk sample, which was surprising given the thickness of the native oxide film. Taking into account that we used a soft $Ar^+$ sputtering conditions ($Ar^+$ 0.5 KeV) to protect the sample from any changes, it could be assumed that a longer sputtering time should have been required to reach the bulk sample. Nevertheless, another hypothesis would be that the bombardment could also promote some level of oxidation on the surface of the alloy.

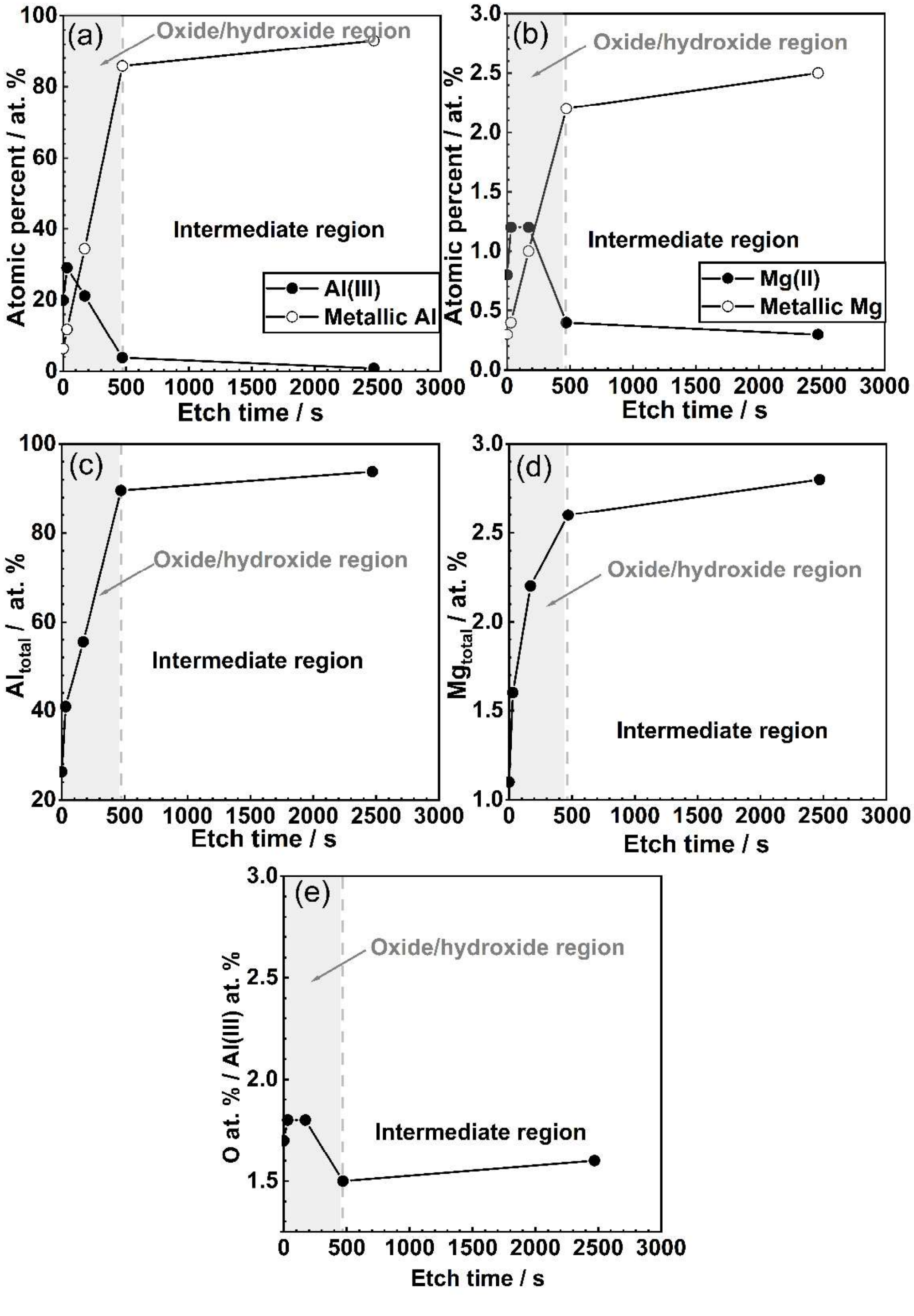

**Figure 5.** Semi-quantitative analysis of the XPS data obtained for the as-polished 1 mm L-LT sample. Concentration profiles (in at. %) plotted for a) Al(III) and metallic Al, b) Mg(II) and metallic Mg as a function of the sputtering time. Total amounts (in at. %) of c) Al and d) Mg as a function of the sputtering time e) Variation of the ratio O/Al(III) as a function of the sputtering time.

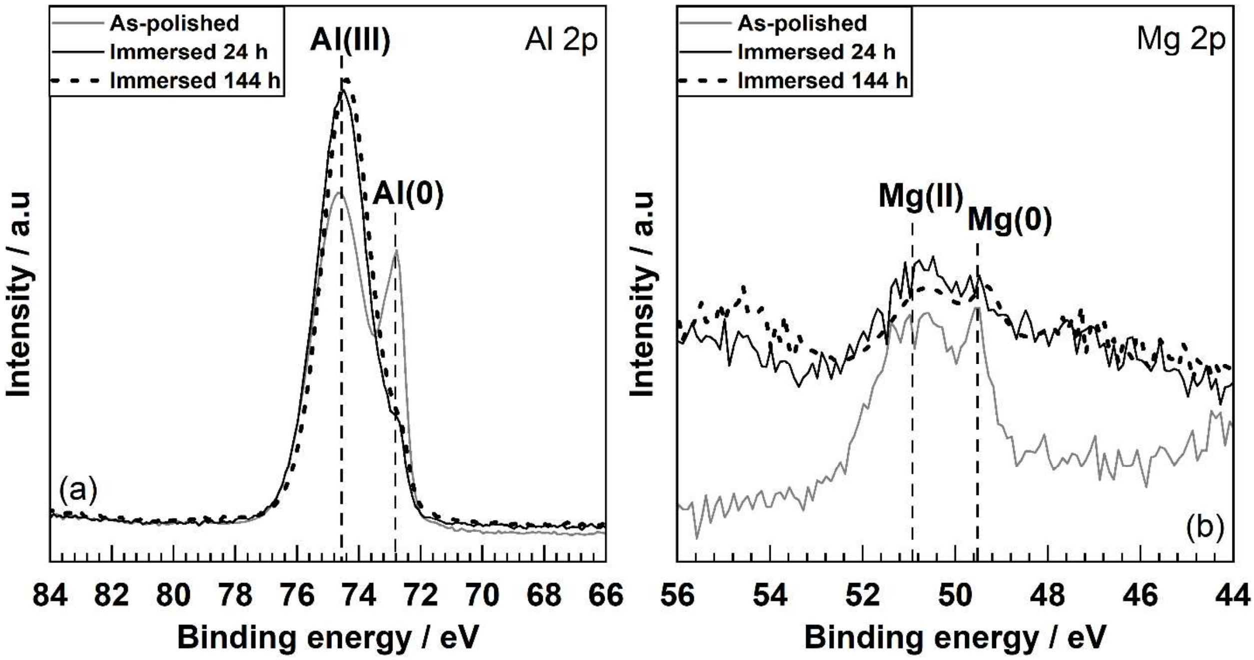

**Figure 6.** XPS analyses of the 1 mm L-LT samples immersed in 0.1 M $Na_2SO_4$ + 0.001 M NaCl for 24 h and 144 h. Results obtained for the as-polished 1 mm L-LT sample are reported for comparison. High resolution a) Al 2p and b) Mg 2p core level spectra.

Fig. 6 shows the high resolution Al 2p (Fig. 6 a)) and Mg 2p (Fig. 6 b)) core level spectra obtained for the samples after immersion in the chloride-containing sulphate solutions for 24 h and 144 h (6 days), allowing the passive films formed on the sample surface to be analysed. The results obtained for the as-polished sample are also reported for comparison. After immersion, independently of the immersion times, the spectra in the Al 2p region also showed a low binding energy component associated to metallic Al and a high binding energy component associated to Al(III) (Fig. 6 a)). However, the intensity of the Al(III) component was higher after immersion compared to the as-polished sample, while that of the metallic component was lower. This showed a thickening of the oxide/hydroxide layer during the immersion in the electrolyte, even if the detection of the metallic Al component revealed the presence of local areas where the passive film was thinner. In the Mg 2p region (Fig. 6 b)), a low binding energy component assigned to metallic Mg and a higher binding energy component assigned to Mg(II) were still detected: this showed that the passive films formed in this electrolyte also incorporated magnesium species, *i.e.* oxy-hydroxides, in agreement with literature [48,49].

However, whatever the immersion times, a significantly weaker signal was measured in the Mg 2p region after immersion in the electrolyte compared to the as-polished sample, showing the dissolution of Mg oxide/hydroxide during the immersion in the electrolyte, and also probably the dissolution of metallic Mg in the underlying alloy [47].

Fig. 7 shows the concentration profiles as a function of the sputtering time plotted for the samples immersed for 24 h and 144 h in the electrolyte. The results obtained for the as-polished sample are reported for comparison. First, the global shape of the curves was similar for the samples immersed for 24 h and 144 h in the electrolyte. Then, comparison of the curves plotted for the samples immersed in the electrolyte with those of the as-polished sample showed that a description of the passivated surfaces with two distinct regions, i.e. oxide/hydroxide region, followed by an intermediate region, could also be proposed as done for the as-polished sample. Here also, the frontiers indicated in Fig. 7 are given as an indication only. Independently of the immersion times, the concentrations of Al(III) (Fig. 7 a)) and Mg(II) (Fig. 7 b)) were about 30 at. % and 0.5 at. %, respectively, in the first region assigned to the oxi/hydroxide film and extending in the range [0 – 470] s of sputtering. The range [470 – 2470] s of sputtering was assigned to the intermediate region, mixing the inner part of the passive film and the bulk sample region; in this region, the Al(III) and Mg(II) concentrations slowly decreased to reach values of about 8.4 at. % and 0.1 at. %, respectively, after 2470 s of sputtering. It could be observed that the total amounts of Al (Fig. 7 c)) and Mg (Fig. 7 d)) did not reach stable values even after 2470 s of sputtering. Additional XPS analyses (not shown) performed for the samples immersed for 24 h between 2470 and 6000 s of sputtering showed a stabilisation of the total Al and Mg amounts for sputtering times higher than 2600 s, whereas, for the native oxide film, the stabilisation occurred after 500 s. Therefore, the results confirmed previous conclusion drawn from the analysis of Fig. 6 a), *i.e.* a thickening of the overall oxi/hydroxide film during the immersion in the chloride-containing sulphate solution compared to the native oxide film, even though the roughness of the surface did not allow proper estimation of the oxi/hydroxide film thickness.

Independently of the immersion times, in the first region assigned to the outer layer of the passive films, the ratio O/Al strongly evolved as observed for the native oxide film: it was about 2 during the first times of sputtering, and then decreased to 1.7 after 500 s of sputtering. Such a ratio could be assigned to AlO(OH), but the analysis was not accurate enough to precisely identify the hydroxylated Al species, and the presence of $Al(OH)_3$ in the outer layer of the passive film could not be neglected as well as the presence of $Al_2O_3$. Nevertheless, the results showed that the outer layer of the passive films was more hydroxylated than that of the native oxide film. In the intermediate region, the O/Al ratio was more stable even if it slowly decreased to 1.5, showing that the inner layer of the passive films was mostly composed of Al oxide ($Al_2O_3$), as observed for the native oxide film. Finally, Fig. 7 b) clearly showed that the concentration of Mg(II) was lower in the inner layer of the passive films than in the outer layer, as observed for the native oxide film. Furthermore, globally over the whole thickness of the passive films (and at least, over 1500 s of sputtering), the concentration of Mg(II) was lower for the immersed samples compared to the as-polished sample showing the dissolution of Mg oxide/hydroxides during the immersion in the electrolyte. Similarly, the concentration of metallic Mg was significantly lower for the immersed samples compared to the as-polished samples. After 2470 s of sputtering, the concentration of metallic Mg in the immersed samples was only 2 at. %, to be compared to 2.5 % for the as-polished sample for the same sputtering time, and 4.8 at. % in the bulk metal. This confirmed also the dissolution of Mg from the underlying metal during the immersion in the chloride-containing sulphate solutions.

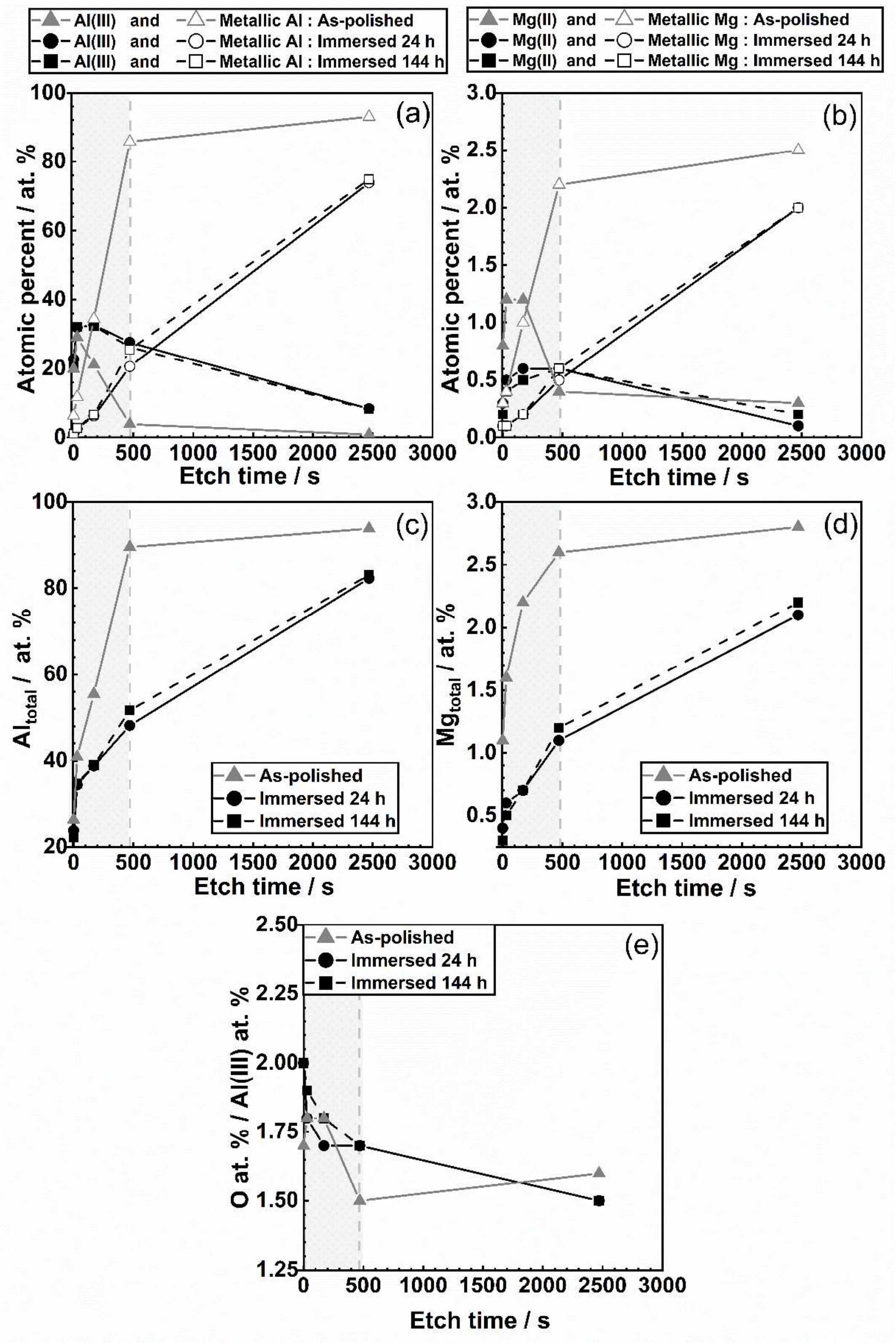

**Figure 7.** Semi-quantitative analysis of the XPS data obtained for the 1 mm L-LT samples immersed in 0.1 M $Na_2SO_4$ + 0.001 M NaCl for 24 h and 144 h. Results obtained for the as-polished sample are reported for comparison. Concentration profiles (in at. %) plotted for a) Al(III) and metallic Al, b) Mg(II) and metallic Mg as a function of the sputtering time. Total amounts (in at. %) of c) Al and d) Mg as a function of the sputtering time. e) Variation of the ratio O/Al(III) as a function of the sputtering time.

The XPS results clearly evidenced the strong reactivity of Mg from the 5083 Al alloy during the immersion in the chloride-containing sulphate solutions in such a way that our hypothesis concerning the attribution of the capacitive loop at high frequency to anodic faradic processes linked to Mg dissolution seemed relevant. It also seemed reasonable to propose that Mg was incorporated into the passive films due to anodic dissolution processes associated with both Mg in solid solution and Mg from the Mg-rich particles, in agreement with literature data [12,13,18,35]. However, as previously indicated, literature data also showed that Mg-rich particles constituted very active sites where the passive film was disrupted, which suggested a strong contribution of the Mg-rich particles to the Mg incorporation into the passive film [18,35]. In the following, in order to model the EIS data, the passive film formed above the matrix was described as mostly composed of alumina. Moreover, in agreement with Aballe *et al.* [18], it was assumed that there were oxide-free zones at the Mg-rich IMCs before immersion; then, during immersion, Mg-rich particles strongly dissolved and were covered by oxi/hydroxides Mg corrosion products. Finally, it was important to note that the XPS results showed a gradient in the chemical composition of the passive films, with clear distinction between a hydroxylated outer layer and an inner layer mostly composed of the Al oxide form. This suggested a gradient in electrical properties, which led us to take advantage of the analysis of the EIS data to plot the resistivity profiles of the passive films.

### 3.3. Modelling of the EIS data

Based on previous conclusions drawn from XPS results and showing that the corrosion behaviour of the 5083 Al alloy was significantly influenced by Mg dissolution at Mg-rich IMCs, we decided to use the model developed by Baril *et al.* concerning Mg dissolution [50], and then discussed by some of the co-authors [51,52], to describe the corrosion behaviour of 5083 Al alloy in chloride-containing sulphate solution. The equivalent electrical circuit used is shown in Fig. 8. It included the electrolyte resistance $R_e$ in series with three other electrical components in parallel, *i.e.* $Z_{ox}$, $Z_F$ and $C_{dl}$ as described here after.

The passive film formed on the matrix was described as a dielectric layer characterised by an impedance $Z_{ox}$. As previously indicated, it was assumed to be composed of mostly Al oxi-hydroxides, without neglecting Mg species, and to be homogeneous in a plane parallel to the surface. However, as shown by XPS results, a gradient in chemical composition had to be taken into account in the direction normal to the sample surface. This led us to consider a gradient in resistivity from the electrolyte/passive film interface to the passive film / underlying alloy interface. Because EIS results (Fig. 2) showed a CPE behaviour in the [1 – 100] Hz frequency range, $Z_{ox}$ had to be described using the power-law model [24]. Therefore, it was given by:

$$Z_{ox=} K / \left[ (\rho_0^{-1} + jw\varepsilon\varepsilon_0)^{\alpha} \right] \qquad \text{Eq. 1}$$

where K and $\alpha$ are two parameters which correspond to the CPE behaviour of the oxide impedance, $\rho_0$ is the resistivity of the passive film at the passive film/underlying alloy interface, $\varepsilon$ is the dielectric constant (assumed to be equal to 11.5 as previously said), and $\varepsilon_0$ is the permittivity of vacuum.

Mg dissolution at Mg-rich IMCs, leading to the production and accumulation of Mg oxi/hydroxides corrosion products, was described by a faradic impedance $Z_F$, so that $Z_F$ was given by the following equations from the work of Baril *et al.* [50]:

$$Z_F = R_{ct} + Z_d + [(K_1 * Z_d + B)/(jw + C_2)] \qquad \text{Eq. 2}$$

where $Z_d = R_d * th[(jwt_1)^{0.5}]/(jwt_1)^{0.5}$ Eq. 3

with, $R_{ct}$ the charge transfer resistance characteristic of Mg dissolution, $Z_d$ and $R_d$ the impedance and resistance, respectively, linked to the diffusion of $Mg^{2+}$ ions through the Mg hydroxide layer, while $K_1$, B, $C_2$ are defined from [50].

Finally, the circuit also included the double layer capacitance $C_{dl}$ assumed to be negligible compared to $Z_{ox}$. With this assumption, the impedance Z of the electrochemical system was given by:

$$Z = R_e + \left[\frac{1}{(\frac{1}{Z_{ox}}+\frac{1}{Z_F})}\right] \qquad \text{Eq. 4}$$

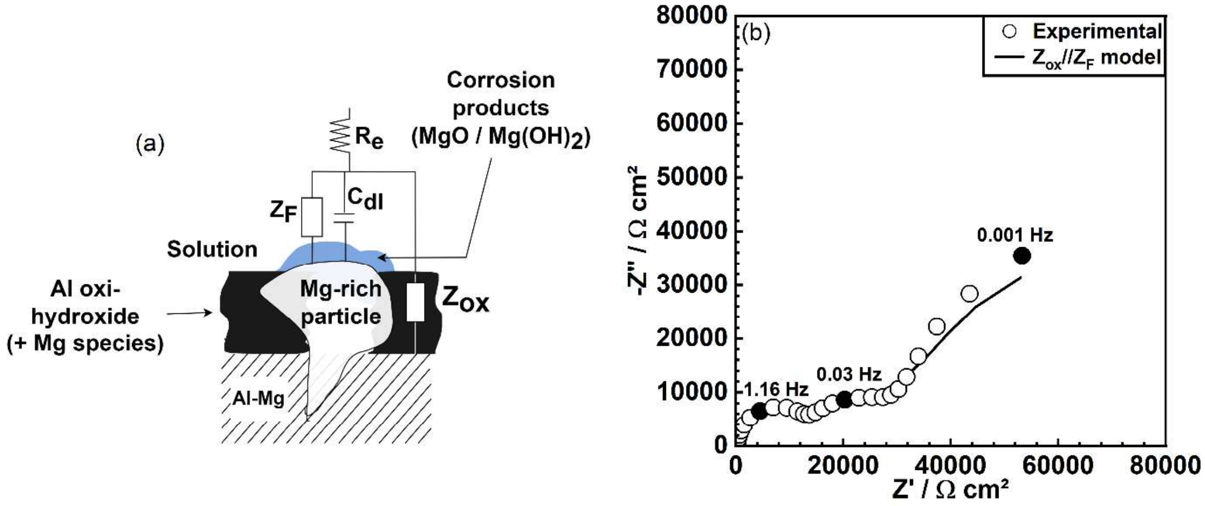

**Figure 8.** a) Equivalent electrical circuit used to model the EIS data, from [50]. The model is referred to as $Z_{ox}//Z_F$ model. b) Experimental impedance data (Nyquist coordinates) obtained for the 1 mm L-LT sample after 24 hours of immersion in 0.1 M $Na_2SO_4$ + 0.001 M NaCl, with the black line corresponding to the fitted $Z_{ox}//Z_F$ model.

This model, referred to as $Z_{ox}//Z_F$, was regressed to all the experimental data previously shown (Fig. 1). As a representative example, Fig. 8 b) reports the experimental impedance data

(Nyquist coordinates) obtained for the 1 mm L-LT sample after 24 hours of immersion in the chloride-containing solution, with the black line corresponding to the fitted $Z_{ox}//Z_F$ model. Results clearly showed that the fit with the $Z_{ox}//Z_F$ model was quite good. All the parameters extracted (using Simad Software) from the model for these EIS data are summarised in Table 2, with the standard deviation indicated. It could be first noted that $\rho_0$ values are not given since first regressions showed that $\rho_0^{-1}$ could be neglected in Eq. 1, which was expected since the capacitive loop at high frequency had been attributed to an anodic faradic process (Fig. 3). Therefore, $\rho_0$ was fixed to $10^{13}$ Ω cm. Then, it was also of interest to note that the standard deviations were quite acceptable for most parameters. Similar results were obtained for all the EIS data shown in Fig. 1. Therefore, considering that the $Z_{ox}//Z_F$ model was based on XPS analyses of the passive films, such a good superimposition between experimental and fitted data led us to conclude that this model could be considered as a physically meaningful model to describe the corrosion behaviour of 5083 Al alloy in chloride-containing sulphate solution. In the following, we chose to consider only two parameters, i.e. $R_{ct}$ values characteristic of the corrosion kinetics (Mg dissolution), and α values which were representative of the homogeneity of the passive films formed on the matrix. The evolution as a function of the immersion time in the electrolyte of the parameters linked to the diffusion of $Mg^{2+}$ ions through the Mg hydroxide layer was not analysed below. Indeed, a main issue was that this hydroxide layer was not really stable and adherent. It evolved from one sample to another, and even for a given sample it evolved as the immersion time in the electrolyte increased. This was clearly shown with the non-monotonous variation in the size of the capacitive loop at high frequency with an increase in the applied potential (Fig. 3). The position of the samples in the electrochemical cell (they were positioned vertically in the electrochemical cell) probably contributed to this effect, as corrosion products could detach from the surface during the immersion. Therefore, the evolution of those parameters as a function of the immersion time in the electrolyte did not lead to meaningful results.

**Table 2.** All the parameters extracted (using Simad Software) from the $Z_{ox}//Z_F$ model (with the standard deviation indicated) for EIS data obtained for the 1 mm L-LT sample after 24 hours of immersion in 0.1 M $Na_2SO_4$ + 0.001 M NaCl.

| | K $\Omega^{1-\alpha}$ $cm^{2-\alpha}$ | α | $R_{ct}$ Ω $cm^2$ | $R_e$ Ω $cm^2$ | $R_d$ Ω $cm^2$ | $t_l$ s | $K_l$ $s^{-1}$ | B Ω $cm^2$ $s^{-1}$ | $C_2$ $s^{-1}$ |
|---|---|---|---|---|---|---|---|---|---|
| Parameters values | $8.01\ 10^{-7}$ | 0.92 | 16425 | 165 | 70 | 664 | 730 | 2849 | 0.62 |
| Standard deviation (%) | 2.4 | 0.1 | 2.8 | 2.02 | 4.9 | 9.2 | 4.9 | 15.2 | 4.3 |

Fig. 9 a) shows the capacitance values at infinite frequency C extracted from the measurement model for 1 mm L-LT, 7 mm L-LT and 7 mm LT-ST samples after 24 h, 72 h, 168 h and 336 h of immersion in the electrolyte. The thickness of the passive film δ formed above the matrix (Fig. 9 b)) was given by:

$$\delta = \frac{\varepsilon\varepsilon_0}{C} \qquad \text{Eq. 5}$$

Parameters extracted from the $Z_{ox}//Z_F$ model, *i.e.* α and $R_{ct}$ values, are shown in Fig. 9 c) and Fig. 9 d), respectively, for the same samples. Results showed that δ values did not depend significantly on the immersion time for both 1 mm L-LT and 7 mm L-LT samples, which had similar δ values (between 1.5 and 2.1 nm), even though a slight increase in δ values was observed for the 1 mm L-LT sample when the immersion time increased, except for 336 h of immersion. On the contrary, δ values decreased when the immersion time increased for the 7 mm LT-ST samples, in such a way that they were significantly higher for the 7 mm LT-ST samples (between 3 and 4 nm) compared to 1 mm L-LT and 7 mm L-LT samples for short immersion times (24 h and 72 h), and then became almost similar (about 2.5 nm) to that of the two last samples for long immersion times (168 h and 336 h). Such a specific behaviour of the 7 mm LT-ST sample had already been observed in our previous study [16], and explained considering first the higher Mg, Mn and Fe contents in the 7 mm plate compared to the 1 mm plate, and secondly, the higher amount of Al-Fe-Mn and Mg-rich IMCs in the 7 mm LT-ST sample compared to 1 mm L-LT and even 7 mm L-LT samples. The differences in microstructural features might explain differences in the growth kinetics of the passive films, and a higher contribution of Mg species to the passive films formed on the 7 mm LT-ST samples could be relevant with the higher amount of Mg-rich IMCs in this sample. This should contribute to explain the decrease in $\delta$ values when the immersion time increased, by referring to the dissolution of Mg oxi/hydroxides shown by XPS analyses during the immersion in the electrolyte. That said, results also showed that $\alpha$ values associated with the passive film formed above the matrix were similar for all samples, suggesting that the homogeneity of the passive films formed above the matrix for all samples was quite similar. Therefore, it was difficult to give robust conclusions about possible differences in terms of thickness and/or homogeneity of the passive films formed above the 1 mm and 7 mm samples. However, $R_{ct}$ values were significantly lower for the 7 mm samples (about 20 k$\Omega$ cm$^2$) compared to the 1 mm sample (between 20 and 140 k$\Omega$ cm$^2$). This was in perfect agreement with our previous results that showed higher $i_{corr}$ values for the 7 mm samples compared to the 1 mm sample [16]. The degraded corrosion behaviour of the 7 mm L-LT samples compared to the 1 mm L-LT sample was explained by the higher amount of Mg-rich IMCs in the 7 mm samples compared to the 1 mm sample. The results obtained in the present study therefore strengthened the conclusion that the corrosion behaviour of the 5083 Al alloy was controlled by processes occurring at a very local scale, *i.e.* anodic dissolution processes at the Mg-rich IMCs.

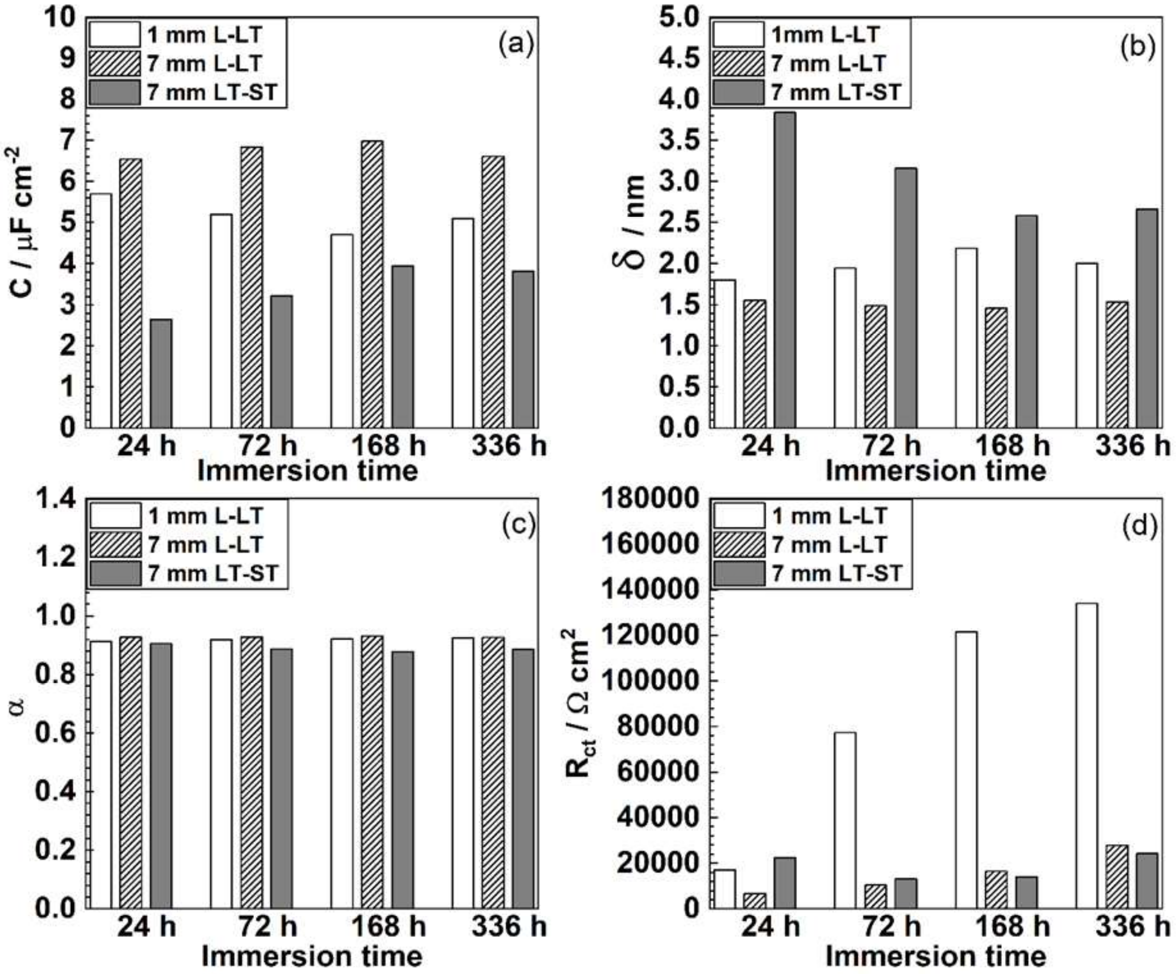

**Figure 9.** a) Capacitance values at infinite frequency C extracted from the measurement model and b) thickness of the passive film δ formed above the matrix calculated from C. Parameters extracted from the $Z_{ox}//Z_F$ model: c) α and d) $R_{ct}$. Results are given for 1 mm L-LT, 7 mm L-LT and 7 mm LT-ST samples after 24 h, 72 h, 168 h and 336 h of immersion in 0.1 M $Na_2SO_4$ + 0.001 M NaCl.

### 3.4. Resistivity profiles of the passive films

The resistivity profiles ρ(x) = f(x) of the passive films, where x was the distance measured from the underlying alloy/passive film interface, were given by:

$$\rho(x) = \rho_\delta\left(\frac{\rho_\delta}{\rho_0} + \left(1 - \frac{\rho_\delta}{\rho_0}\right)\left(\frac{x}{\delta}\right)^\gamma\right)^{-1} \qquad \text{Eq. 6 [25,53,54],}$$

where $\rho_\delta$ was the passive film resistivity at the electrolyte/passive film interface, and:

$$\gamma = \frac{1}{1-\alpha} \qquad \text{Eq. 7,}$$

$$K = g\delta\rho_\delta^{1-\alpha} \qquad \text{Eq. 8,}$$

and $g = 1 + 2.88(1-\alpha)^{2.375}$ Eq. 9

Based on α and K values previously extracted from the $Z_{ox}//Z_F$ model, and δ values calculated from C values extracted from the measurement model, the resistivity profiles of the passives films formed on all samples were then calculated. First, Fig. 10 shows that the resistivity profiles plotted in semi-logarithmic coordinates had similar shape for all samples independently of the immersion times in the electrolyte. A plateau at a value of resistivity of $\rho_0$ was first observed, followed by a slow decrease of the resistivity when going to the passive film/electrolyte interface. This means that the resistivity remained that of an insulator over a distance of about 1 nm, and then progressively decreased until the passive film/electrolyte interface was reached. Such an evolution of the resistivity of the passive films was in good agreement with previous conclusions drawn from XPS analyses showing that the passive films were constituted of an almost homogeneous inner layer, mostly composed of $Al_2O_3$, and an outer layer mixing oxide and hydroxides and characterised by a gradient in chemical composition. It was of interest to highlight that the resistive profiles deduced from EIS data not only fitted very well the double-layer structure of the passive films, but also confirmed the homogeneity of their inner layer, while highlighting the heterogeneity of their outer layer. Therefore, this strengthened the conclusion that the $Z_{ox}//Z_F$ model was a physically meaningful model to describe the corrosion behaviour of the 5083 Al alloy in chloride-containing sulphate solution.

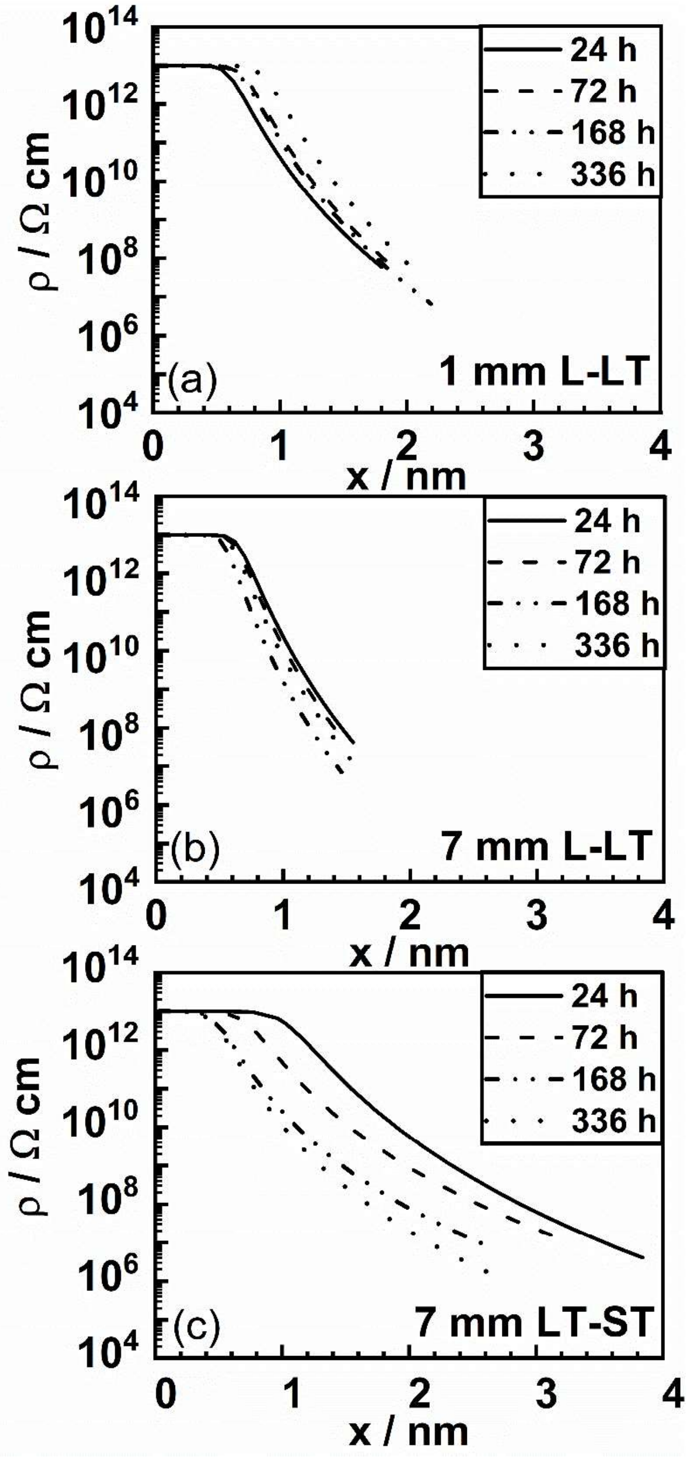

**Figure 10.** Resistivity profiles plotted for the passive films formed on 1 mm L-LT, 7 mm L-LT and 7 mm LT-ST samples after 24 h, 72 h, 168 h and 336 h of immersion in 0.1 M $Na_2SO_4$ + 0.001 M NaCl.

Then, despite of a similar global shape for all the resistivity profiles, results showed differences between the 1 mm L-LT sample and the 7 mm samples, as expected from the previously observed evolution of δ values (Fig. 9 b)). For the 1 mm sample, a global shift of the resistivity profiles was observed towards higher x values when the immersion time in the electrolyte was increased, with an increase in the length of the plateau at high resistivity value. This suggested a progressive thickening of the passive film formed on the 1 mm L-LT sample during immersion in the electrolyte, in agreement with XPS results. On the contrary, for the 7 mm samples, in particular the 7 mm LT-ST sample, the resistivity profiles suggested a thicker passive film whose thickness decreased when the immersion time increased. However, as previously said, it was difficult to propose strengthened conclusions on this specific point.

## 4. Conclusions

The present study proposed a combined EIS and XPS analysis of the corrosion behaviour of the 5083 Al alloy, that completed the previous approach we had using potentiodynamic polarisation curves [16]. The main results are the following:

1. EIS diagrams of the 1 mm and 7 mm samples showed three capacitive loops, attributed to an anodic faradic process, assumed to be linked with Mg dissolution at Mg-rich IMCs.
2. XPS analysis revealed a double-layer structure of the passive films: an outer layer composed of Al oxi-hydroxides and including Mg-rich species, with a gradient in chemical composition in the direction normal to the surface, and a more homogeneous inner layer, mostly composed of $Al_2O_3$, with a reduced amount of Mg species.
3. The rigorous and combined analysis of EIS and XPS data allowed to propose a model, based on the work of Baril *et al.* [50], that included an impedance of the passive film in parallel with a charge transfer resistance characteristic of the Mg dissolution. Results showed that the experimental data and the fitted ones were very-well superimposed, confirming that the corrosion behaviour or 5083 Al alloy was controlled by processes occurring at the Mg-rich IMCs.

4. The results also confirmed our previous conclusions that 7 mm L-LT samples were less resistant to corrosion than 1 mm L-LT sample [16], due to the higher amount of Mg-rich IMCs.
5. Finally, the model also allowed to plot the resistivity profiles of the passive films. Results showed that the resistivity profiles very well highlighted the double-layer structure of the passive films, and confirmed the homogeneity of the inner layer, while demonstrating the gradient in chemical composition of the outer layer. Such a result strengthened the conclusion that the model developed was physically meaningful.

## Acknowledgments

This work was financially supported by the ANR, in the framework of the MICOATEC project (ANR-19-CE08-0018).

### *Data availability*

The raw/processed data required to reproduce these findings cannot be shared at this time as the data also forms part of an ongoing study.

## Credit authorship contribution statement

**C. Nkoua**: Investigation, Formal analysis, Validation, Visualization, Methodology, Data curation, Writing - review & editing. **J. Esvan**: Investigation for XPS analyses, Formal analysis for XPS analyses, Validation for XPS analyses, Writing - review & editing. **B. Tribollet**: Methodology, Formal analysis, Validation, Visualization, Data curation, Writing -review & editing. **R. Basséguy**: Funding acquisition, Methodology, Formal analysis, Project administration, Supervision, Validation, Conceptualization, Data curation, Writing -review & editing. **C. Blanc**: Funding acquisition, Methodology, Formal analysis, Project administration, Supervision, Validation, Conceptualization, Data curation, Writing - original draft, Writing - review & editing.

## References

[1] S.J. Kim, S.J. Lee, J.Y. Jeong, K.H. Kim, Electrochemical characteristics of Al-Mg and Al-Mg-Si alloy in sea water, Trans. Nonferrous Met. Soc. China (English Ed.) 22 (2012) s881–s886. https://doi.org/10.1016/S1003-6326(12)61820-2.

[2] H. Ezuber, A. El-Houd, F. El-Shawesh, A study on the corrosion behavior of aluminum alloys in seawater, Mater. Des. 29 (2008) 801–805. https://doi.org/10.1016/j.matdes.2007.01.021.

[3] S.J. Kim, M.S. Han, S.K. Jang, Electrochemical characteristics of Al-Mg alloy in seawater for leisure ship: Stress corrosion cracking and hydrogen embrittlement, Korean J. Chem. Eng. 26 (2009) 250–257. DOI: 10.1016/S1003-6326(12)61820-2.

[4] E. Kus, Z. Lee, S. Nutt, F. Mansfeld, A comparison of the corrosion behaviour of nanocrystalline and conventional Al 5083 samples, Corros. 62 (2006) 152–161. https://doi.org/10.5006/1.3278260.

[5] Y. Huang, Y. Li, Z. Xiao, Y. Liu, Y. Huang, X. Ren, Effect of homogenization on the corrosion behavior of 5083-H321 aluminum alloy, J. All. Compd. 673 (2016) 73–79. https://doi.org/10.1016/j.jallcom.2016.02.228

[6] Y. Ding, K. Gao, H. Huang, S. Wen, X. Wu, Z. Nie, S. Guo, R. Shao, C. Huang, D. Zhou, Nucleation and evolution of β phase and corresponding intergranular corrosion transition at 100–230 °C in 5083 alloy containing Er and Zr, Materials & Design, 174 (2019) 107778, https://doi.org/10.1016/j.matdes.2019.107778.

[7] R.G. Buchheit, R.K. Boger, M.C. Carroll, R.M. Leard, C. Paglia, J.L. Searles, The electrochemistry of intermetallic particles and localized corrosion in Al alloys, JOM 53 (2001) 29–33. https://doi.org/10.1007/s11837-001-0084-x.

[8] Y. Li, B. Yang, M. Zhang, H. Wang, W. Gong, R. Lai, Y. Li, J. Teng, The corrosion behavior and mechanical properties of 5083 Al-Mg alloy manufactured by additive friction stir deposition, Corros. Sci. 213 (2023) 110972, https://doi.org/10.1016/j.corsci.2023.110972.

[9] L. Fan, J. Ma, C. Zou, J. Gao, H. Wang, J. Sun, Q. Guan, J. Wang, B. Tang, J. Li, W. Yi Wang, Revealing foundations of the intergranular corrosion of 5XXX and 6XXX Al alloys, Materials Letters, 271 (2020) 127767, https://doi.org/10.1016/j.matlet.2020.127767.

[10] M.-J. Li, S. Liu, X.-D. Wang, Y.-J. Shi, Q.-L. Pan, X.-J. Zhou, R.-F. Zhang, N. Birbilis, Improved intergranular corrosion resistance of Al-Mg-Mn alloys with Sc and Zr additions, Micron, 154 (2022) 103202, https://doi.org/10.1016/j.micron.2021.103202.

[11] G. Yi, D.A. Cullen, K.C. Littrell, W. Golumbfskie, E. Sundberg, M.L. Free, Characterization of Al-Mg alloy aged at low temperatures, Met. Mat. Trans. A, 48A (2017) 2040 –2050. DOI: 10.1007/s11661-017-3992-2.

[12] A. Davoodi, Z. Esfahani, M. Sarvghad, Microstructure and corrosion characterization of the interfacial region in dissimilar friction stir welded AA5083 to AA7023, Corros. Sci. 107 (2016) 133–144. https://doi.org/10.1016/j.corsci.2016.02.027.

[13] K.A. Yasakau, M.L. Zheludkevich, S. V. Lamaka, M.G.S. Ferreira, Role of intermetallic phases in localized corrosion of AA5083, Electrochim. Acta. 52 (2007) 7651–7659. https://doi.org/10.1016/j.electacta.2006.12.072.

[14] W. Gao, D. Wang, M. Seifi, J.J. Lewandowski, Anisotropy of corrosion and environmental cracking in AA5083-H128 Al-Mg alloy, Mater. Sci. Eng. A. 730 (2018) 367–379. https://doi.org/10.1016/j.msea.2018.06.021.

[15] L. Esteves, C.S. Witharamage, J. Christudasjustus, G. Walunj, S.P. O'Brien, S. Ryu, T. Borkar, R.E. Akans, R.K. Gupta, Corrosion behavior of AA5083 produced by high-energy ball

milling, J. Alloys Compd. 857 (2021) 158268. https://doi.org/10.1016/j.jallcom.2020.158268. J. All. Comp.

[16] C. Nkoua, C. Josse, A. Proietti, R. Basseguy, C. Blanc, Corrosion behaviour of the microbially modified surface of 5083 aluminium alloy, Corros. Sci. 210 (2023) 110812. https://doi.org/10.1016/j.corsci.2022.110812.

[17] B. Wang, J. Liu, M. Yin, Y. Xiao, X. H. Wang, J. X. He, Comparison of corrosion behavior of Al-Mn and Al-Mg alloys in chloride aqueous solution, Mat. Corros. 67 (2016) 51–59. DOI:10.1002/maco.201408211.

[18] A. Aballe, M. Bethencourt, F. J. Botana, M. Marcos, R. Osuna, Using EIS to study the electrochemical response of alloy AA5083 in solutions of NaCl, Mat. Werkstoffe und Korrosion 52 (2001) 185–192. https://doi.org/10.1002/1521-4176(200103)52:3%3C185::AID-MACO185%3E3.0.CO;2-O.

[19] S. Scotto-Sheriff, E. Darque-Ceretti, G. Plassart, M. Aucounturier, Physico-chemical characterisation of native air-formed oxide films on Al-Mg alloys at low temperature . Influence of water, Journals Mater. Sci. 4 (1999) 5081–5088. https://dx.doi.org/10.1023/A:1004709032754.

[20] M. Santamaria, F. Di Quarto, S. Zanna, P. Marcus, Initial surface film on magnesium metal: A characterization by X-ray photoelectron spectroscopy (XPS) and photocurrent spectroscopy (PCS), Electrochim. Acta. 53 (2007) 1314–1324. https://doi.org/10.1016/j.electacta.2007.03.019.

[21] M. Liu, S. Zanna, H. Ardelean, I. Frateur, P. Schmutz, G. Song, A. Atrens, P. Marcus, A first quantitative XPS study of the surface films formed, by exposure to water, on Mg and on the Mg–Al intermetallics: $Al_3Mg_2$ and $Mg_{17}Al_{12}$, Corros. Sci., 51 (2009) 1115-1127. https://doi.org/10.1016/j.corsci.2009.02.017.

[22] C. Yao, S. L. Tay, T. Zhu, H. Shang and W. Gao, Effects of Mg content on microstructure and electrochemical properties of Zn–Al–Mg alloys, J. All. Compd. 645 (2015) 131—136. https://doi.org/10.1016/j.jallcom.2015.05.010.

[23] E. Brillas, P. L. Cabot, F. Centellas, J. A. Garrido, E. Perez, R. M. Rodriguez, Electrochemical oxidation of high-purity and homogeneous Al-Mg alloys with low Mg contents, Electrochim. Acta 43 (1998) 799–812. https://doi.org/10.1016/S0013-4686(97)00266-1.

[24] M.E. Orazem, I. Frateur, B. Tribollet, V. Vivier, S. Marcelin, N. Pebere, A.L. Bunge, E.A. White, D.P. Riemer, M. Musiani, Dielectric properties of materials showing constant-phase-element (CPE) impedance response, J. Electrochem. Soc., 160 (2013) C215–C225. https://doi.org/10.1149/2.033306jes.

[25] B. Tribollet, V. Vivier, M. E. Orazem, EIS technique in passivity studies: determination of the dielectric properties of passive films, in Encyclopedia of interfacial chemistry: surface science and electrochemistry, Elsevier, 2017, pp. 1–14.

[26] W. Watson and M. E. Orazem, EIS: Measurement Model Program, ECSArXiv, 2020, https://ecsarxiv.org/kze9x/.

[27] A. Aballe, M. Bethencourt, F.J. Botana, M.J. Cano, M. Marcos, Localized alkaline corrosion of alloy AA5083 in neutral 3.5% NaCl solution, Corros. Sci. 43 (2001) 1657–1674. https://doi.org/10.1016/S0010-938X(00)00166-9.

[28] P. Agarwal, M. E. Orazem, and L. H. García-Rubio, Measurement Models for Electrochemical Impedance Spectroscopy: 1. Demonstration of Applicability, J. Electrochem. Soc., 139 (1992) 1917–1927. https://doi.org/10.1149/1.2069522.

[29] P. Agarwal, O. D. Crisalle, M. E. Orazem, and L. H. García-Rubio, Application of Measurement Models to Electrochemical Impedance Spectroscopy: 2. Determination of the Stochastic Contribution to the Error Structure, J. Electrochem. Soc., 142 (1995) 4149–4158. https://doi.org/10.1149/1.2048478.

[30] P. Agarwal, M. E. Orazem, and L. H. García-Rubio, Application of Measurement Models to Electrochemical Impedance Spectroscopy: 3. Evaluation of Consistency with the Kramers-Kronig Relations, J. Electrochem. Soc., 142 (1995) 4159–4168. https://doi.org/10.1149/1.2048479.

[31] P. Agarwal, O. C. Moghissi, M. E. Orazem, and L. H. Garcia-Rubio, Application of Measurement Models for Analysis of Impedance Spectra, Corrosion, 49 (1993) 278–289. https://doi.org/10.5006/1.3316050.

[32] H. Liao, W. Watson, A. Dizon, B. Tribollet, V. Vivier, M.E. Orazem, Physical properties obtained from measurement model analysis of impedance measurements, Electrochim. Acta, 354 (2020) 136747. DOI : 10.1016/j.electacta.2020.136747.

[33] M. E. Orazem, N. Pébère, B. Tribollet, Enhanced graphical representation of electrochemical impedance data, J. Electrochem. Soc., 153 (2006) B129–B136. DOI: 10.1149/1.2168377.

[34] J.L. Searles, P.I. Gouma, R.G. Buchheit, Stress corrosion cracking of sensitized AA5083 (Al-4.5Mg-1.0Mn), Metall. Mater. Trans. A. 32 (2001) 2859–2867. https://doi.org/10.4028/www.scientific.net/msf.396-402.1437.

[35] F. Eckermann, T. Suter, P.J. Uggowitzer, A. Afseth, P. Schmutz, The influence of MgSi particle reactivity and dissolution processes on corrosion in Al–Mg–Si alloys, Electrochim. Acta. 54 (2008) 844—855. https://doi.org/10.1016/j.electacta.2008.05.078.

[36] E. Juzeliunas, K. Leinartas, W. Fürbeth, K. Jüttner, Study of initial stages of Al–Mg alloy corrosion in water, chloride and Cu(II) environment by a scanning Kelvin probe, Corros. Sci. 45 (2003) 1939–1950. doi:10.1016/S0010-938X(03)00026-X.

[37] T. Tago, N. Kataoka, H. Tanaka, K. Kinoshita, S. Kishida, XPS study from a clean surface of $Al_2O_3$ single crystals, Proc. Eng. 216 (2017) 175–181. https://doi.org/10.1016/j.proeng.2018.02.081.

[38] J. Zähr, S. Oswald, M. Türpe, H.J. Ullrich, U. Füssel, Characterisation of oxide and hydroxide layers on technical aluminum materials using XPS, Vacuum, 86 (2012) 1216-1219, https://doi.org/10.1016/j.vacuum.2011.04.004.

[39] M. Shahabi-Navid, Y. Cao, J.E. Svensson, A. Allanore, N. Birbilis, L.G. Johansson, M. Esmaily, On the early stages of localized atmospheric corrosion of magnesium-aluminium alloys, Scientific reports 10 (2020) 20972. https://doi.org/10.1038/s41598-020-78030-w.

[40] S.J. Splinter, N.S. McIntyre, W.N. Lennard, K. Griffiths, G. Palumbo, An AES and XPS study of the initial oxidation of polycrystalline magnesium with water vapour at room temperature, Surface Science, 292 (1993) 130–144. https://doi.org/10.1016/0039-6028(93)90396-2.

[41] N.S. McIntyre, C. Chen, Role of impurities on Mg surfaces under ambient exposure conditions, Corrosion Science, 40 (1998) 1697–1709. https://doi.org/10.1016/S0010-938X(98)00072-9.

[42] B. Xiao, D. Wang, F. Cheng, Y. Wang, Oxide film on 5052 aluminium alloy: Its structure and removal mechanism by activated CsF–AlF3 flux in brazing, Appl. Surf. Sci. 337 (2015) 208–215. https://doi.org/10.1016/j.apsusc.2015.02.093.

[43] G.R. Wakefield, R.M. Sharp, The composition of oxides formed on Al-Mg alloys, Appl. Surf. Sci. 51 (1991) 95–102. https://doi.org/10.1016/0169-4332(91)90065-R.

[44] F. Cheng, H. Zhao, Y. Wang, B. Xiao, J. Yao, Evolution of surface oxide film of typical aluminum alloy during medium-temperature brazing process, Trans. Tianjin Univ. 20 (2014) 054–059. DOI 10.1007/s12209-014-2236-4

[45] E. Panda, L.P.H. Jeurgens, E.J. Mittemeijer, Growth kinetics and mechanism of the initial oxidation of Al-based Al–Mg alloys, Corros. Sci. 52 (2010) 2556-2564. https://doi.org/10.1016/j.corsci.2010.03.028.

[46] E. Panda, L.P.H. Jeurgens, E.J. Mittemeijer, The initial oxidation of Al-Mg alloys: depth-resolved quantitative analysis by angle-resolved x-ray photoelectron spectroscopy and real-time in situ ellipsometry, J. Appl. Phys. 106 (2009) 114913. Doi: 10.1063/1.3268480.

[47] R. Saillard, S. Zanna, A. Seyeux, B. Fori, J. Swiatowska, C. Blanc, P. Marcus, Influence of copper on the corrosion behaviour of a 2024 aluminium alloy coated with a trivalent chromium conversion layer, Corros. Sci. 182 (2021) 109192. https://doi.org/10.1016/j.corsci.2020.109192.

[48] M. Elboujdaini, E. Ghali, R. G. Barradas, M. Girgis, An electrochemical investigation of the behaviour of aluminum alloys in different electrolytes, Corros. Sci. 30 (1990) 855–867. https://doi.org/10.1016/0010-938X(90)90009-T.

[49] L. Esteves, J. Christudasjustus, S.P. O'Brien, C.S. Witharamage, A.A. Darwish, G. Walunj, P. Stack, T. Borkar, R.E. Akans, R.K. Gupta, Effect of V content on corrosion behavior of high-energy ball milled AA5083, Corros. Sci. 186 (2021) 109465. https://doi.org/10.1016/j.corsci.2021.109465.

[50] G. Baril, G. Galicia, C. Deslouis, N. Pébère, B. Tribollet, V. Vivier, An Impedance Investigation of the Mechanism of Pure Magnesium Corrosion in Sodium Sulfate Solutions, J. Electrochem. Soc. 154 (2007) C108–C113. DOI: 10.1149/1.2401056.

[51] A.Z. Benbouzid, M. Pereira Gomes, I. Costa, O. Gharbi, N. Pébère, J.L. Rossi, M.T.T. Tran, B. Tribollet, M. Turmine, V. Vivier, A new look on the corrosion mechanism of magnesium: An EIS investigation at different pH, Corros. Sci., 205 (2022) 110463. https://doi.org/10.1016/j.corsci.2022.110463.

[52] M. Pereira Gomes, I. Costa, N. Pébère, J.L. Rossi, B. Tribollet, V. Vivier, On the corrosion mechanism of Mg investigated by electrochemical impedance spectroscopy, Electrochim. Acta. 306 (2019) 61–70, https://doi.org/10.1016/j.electacta.2019.03.080.

[53] B. Hirschorn, M. E. Orazem, B. Tribollet, V. Vivier, I. Frateur, M. Musiani, Constant-Phase-Element Behavior Caused by Resistivity Distributions in Films I. Theory, J. Electrochem. Soc., 157 (2010) C452-C457. DOI: 10.1149/1.3499564.

[54] B. Hirschorn, M. E. Orazem, B. Tribollet, V. Vivier, I. Frateur, M. Musiani, Constant-Phase-Element Behavior Caused by Resistivity Distributions in Films II. Applications, J. Electrochem. Soc., 157 (2010) C458-C463. DOI: 10.1149/1.3499565.